Numerical analysis of tips in viscous flow

J. Eggers[1] and S. Courrech du Pont[2]
[1]*School of Mathematics, University of Bristol, University Walk, Bristol BS8 1TW, United Kingdom*
[2]*Laboratoire Matière et Systèmes Complexes, Université Paris Diderot, CNRS UMR 7057, 10 rue Alice Domon et Léonie Duquet, 75205 Paris Cedex 13, France*

(Received 29 October 2008; revised manuscript received 17 May 2009; published 19 June 2009)

When a drop (or gas bubble) is placed in a strong viscous flow (e.g., a shear flow), it develops very sharp tips at its ends. Sharp tips are also formed when a viscous fluid is withdrawn from the neighborhood of its interface with the ambient air or with another fluid (selective withdrawal). However, it is observed frequently that there exists a critical flow strength above which the drop transitions toward a "jetting state" in which a jet comes out from the tip. In this paper, we look numerically for stationary drop shapes, both globally and close to the tip, which we study with very high resolution. To this end we use a boundary integral method to solve the axisymmetric flow equations for arbitrary viscosity ratios in the inertialess (Stokes) limit. Stationary states are solved for using Newton's method. This permits us to find both stable and unstable steady states and to investigate the nature of the jetting transition. The critical parameters for this transition are in reasonable agreement with slender-body theory. Excellent agreement is found with our earlier experiments in the selective withdrawal geometry [S. Courrech du Pont and J. Eggers, Phys. Rev. Lett. **96**, 034501 (2006)], for which the viscosity of the phase inside the tip is negligible. We describe a scale invariance of the experimental interface profiles away from the tip. Then we investigate the highly curved tip region not considered previously with comparable precision. We find that the shape near the tip is universal, i.e., independent of the outer flow and of the geometry of the system (drop or selective withdrawal). While the tip curvature becomes extremely large, it always remains finite if surface tension is present.

DOI: 10.1103/PhysRevE.79.066311 PACS number(s): 47.20.Ma

I. INTRODUCTION

Free surfaces are likely to develop very sharp tips if they are subject to a strong external flow. This was first demonstrated by Taylor [1], by placing a liquid drop of small viscosity in a viscous flow produced by counter-rotating rollers, stretching the drop in an elongational flow; see Fig. 1. At its ends, the drop develops tips which become quite sharp, yet it is not known on which scale the tip is rounded, if at all [3]. In the selective withdrawal experiment on the right-hand side of Fig. 1, the free surface is deformed by a sink flow and again a sharp tip forms. Thus there exists a generic mechanism by which very small scales are produced, owing to the nonlinear properties of the hydrodynamic equations, without a need for microfabrication. If the tip becomes unstable it may produce extremely thin jets [4–8], which have numerous microfluidic applications [4,9,10].

A variety of other free-surface flows also develop singularities under sufficiently strong forcing. For example, two-dimensional versions of the Stokes flows considered here develop a cusp, but which is regularized by surface tension [11]. The same type of cusp is found in Hele-Shaw flow [12] and numerical solutions suggest regularization by surface tension [13]. An axisymmetric analog of the Hele-Shaw system (the porous medium equation) was studied in [14], giving similar results. Finally, cusps are found for *inviscid* potential flow with a free surface [15,16] but vanishing surface tension. In the following, we will make frequent comparisons between the three-dimensional axisymmetric Stokes flow studied in the present paper and its two-dimensional counterpart. While there are some superficial similarities, the scaling and stability properties of the two problems are rather different.

A theory for the stationary shape of drops and their transition toward a jetting state was developed by Taylor [17], who also provided the first experimental observations [1], and refers to the phenomenon as "tip streaming." The basic idea, worked out in much greater detail in subsequent papers [18–21], is that the drop can be represented as a line distribution of two-dimensional sources, which can be computed using the slenderness of the drop as a small parameter. It is straightforward to add the effect of the fluid inside the drop, in the limit that its viscosity is small compared to that of the exterior [17]. As a result, pressure builds up near the end of the drop, until a closed shape can no longer be sustained. The smaller the viscosity, the stronger the flow required for the drop to burst. It was one of the main surprises of the experiment [5] in the selective withdrawal geometry that this transition was found to be almost unaffected by the viscosity ratio [6] contradicting the above theoretical ideas. Numerical simulations of pointed drop shapes have been around for a long time [8,22–25]. However, past studies were not able to resolve the tip region with an accuracy sufficient to address the above issues.

In the next section, we describe in detail the boundary integral code [26] that permits us to calculate stable and unstable stationary states of free surfaces in an external flow in the Stokes limit. Special care is taken to resolve the extremely high curvatures that occur on the symmetry axis of both flows. In the third section we describe Taylor's classical theory for the shape and stability of drops in various external flow fields and compare to numerical simulations. In the following section we explain the modifications to the code necessary to describe the selective withdrawal geometry and investigate tip stability numerically. In the fifth section we present a detailed comparison to previous selective with-

 ©2009 The American Physical Society

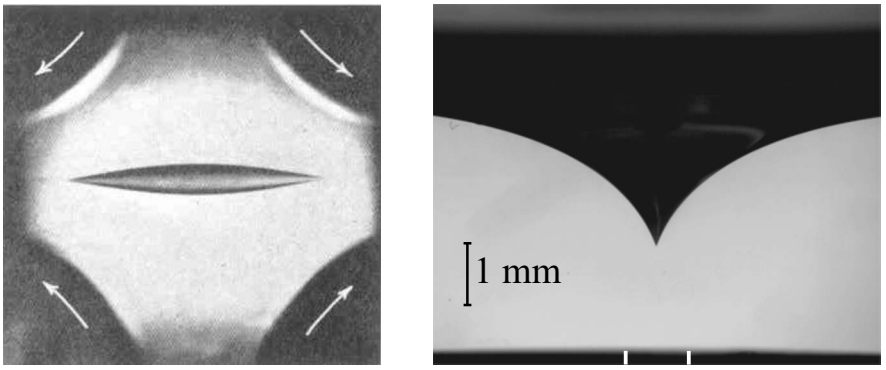

FIG. 1. On the left, a drop of low-viscosity fluid (a mixture of CCl_4 and paraffin) is stretched in Taylor's "four-roller" machine [1], filled with viscous fluid (golden syrup mixed with water). Very sharp tips form at the end, while the drop remains stable. On the right, the air-liquid surface of a container draining from a hole in the bottom [2]. The liquid is very viscous silicone oil.

drawal experiments, both for liquid-liquid and liquid-gas systems, and find excellent agreement, except for the stability properties observed in [6], as mentioned above. We also describe a scaling property of experimentally measured profiles, which relates profiles at different flow strengths and permits to make contact with Taylor's slender-body theory. In the penultimate section we study the tip region and show that it is described by scaling laws which hold for both drops and for selective withdrawal. In the final discussion we point out various unresolved problems.

II. NUMERICS

A. Boundary integral

We confine ourselves entirely to a low Reynolds number (Stokes) regime, where inertial effects can be disregarded. This is a good approximation for many experiments, both on drops and in the viscous withdrawal geometry. The most effective numerical description of such a system is that of the boundary integral method [23,27], but other methods, such as an accurate boundary element code [8], have also been considered for similar problems. Our aim is to provide a detailed numerical description of the highly curved tip region. The key ingredients of our numerical code are the following:

(1) a high order approximation of the free interface;
(2) subtraction of singularities;
(3) a highly nonuniform grid, which permits very high resolution near tips;
(4) a Newton scheme that assures second-order convergence toward the fixed point solution;
(5) efficient continuation as function of a variety of parameters such as the capillary number or the total drop length.

In previous work on pointed drops [28], a very low resolution was used and no effort was made to resolve the tip. In [23], more points are used to represent the surface, but the tip resolution remains limited to a maximum reported tip curvature of 10^2 in units of the drop radius. By contrast, the present code resolves tip curvatures of up to 10^9, with very little error as measured by the residual normal velocity of the interface.

Let us formulate the problem first for the case of a drop in an external flow field [3]. Let the (time-dependent) surface of the drop be $S(t)$, the viscosity of the exterior fluid η, and the viscosity of the drop $\lambda\eta$. The velocity field can be expressed as an integral equation involving the surface forces $\gamma\kappa\mathbf{n}$, where $\mathbf{n}$ is the normal vector directed into the outer fluid and $\kappa=\nabla\cdot\mathbf{n}$ is the curvature of the interface. We make the velocity dimensionless with respect to the capillary velocity γ/η, all lengths with respect to the *unperturbed* drop radius R, and times with respect to the corresponding time scale $\tau=R\eta/\gamma$.

Calculation of the evolution of the interface $S(t)$ requires only the interfacial velocity, which is given by the integral equation [27]

$$\frac{(1+\lambda)}{2}\mathbf{u}(\mathbf{x}_1) = -\int_S \kappa\mathbf{J}\cdot\mathbf{n}d\sigma_2 + (\lambda-1)\int_S \mathbf{u}\cdot\mathbf{K}\cdot\mathbf{n}d\sigma_2 + \mathbf{u}^{(ext)}(\mathbf{x}_1). \quad (1)$$

The integral kernels $\mathbf{J}$ and $\mathbf{K}$ [29] describe the response of the flow field and of the stress tensor to a point forcing:

$$\mathbf{J}(\mathbf{r}) = \frac{1}{8\pi}\left[\frac{\mathbf{I}}{r}+\frac{\mathbf{rr}}{r^3}\right], \quad \mathbf{K}(\mathbf{r}) = -\frac{3}{4\pi}\frac{\mathbf{rrr}}{r^5}, \quad \mathbf{r}=\mathbf{x}_1-\mathbf{x}_2. \quad (2)$$

The points $\mathbf{x}_1$ and $\mathbf{x}_2$ both lie on $S(t)$ and $d\sigma_2$ denotes a surface area element at position $\mathbf{x}_2$. The first term on the right-hand side of Eq. (1) represents the driving by the surface forces, the second accounts for the difference in viscosity between the fluids, and the third comes from the external flow. The problem is closed by requiring that any material marker m with position $\mathbf{x}_1$ on the surface moves according to

$$\partial_t\mathbf{x}_1(m) = \mathbf{u}(\mathbf{x}_1). \quad (3)$$

B. Subtraction of singularities

All problems considered in this paper possess cylindrical symmetry, so the azimuthal integrations in Eq. (1) can be performed analytically; see [26] for the explicit expressions in terms of elliptic integrals. The remaining numerical task is to perform a line integral over the contour of the drop and to

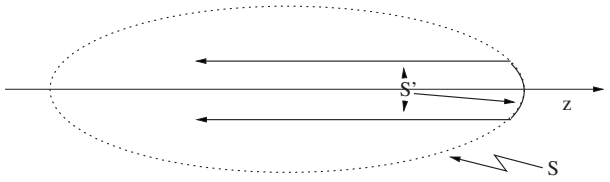

FIG. 2. Schematic of the subtraction procedure. The surface S is the drop, S' is defined to be identical to S in a small region around the tip, and a cylinder extending to infinity away from the tip.

solve the resulting integral equation for the velocity on the contour. The kernel of the line integrals contain logarithmic singularities, which are quite tedious to remove. An elegant way to subtract the singularity to leading order was proposed by [24], using the exact relationships [28]

$$\frac{1}{2}\mathbf{I} = \int_S \mathbf{n} \cdot \mathbf{K} d\sigma_2 \tag{4}$$

and

$$\int_S \mathbf{J} \cdot \mathbf{n} d\sigma_2 = 0. \tag{5}$$

Using Eqs. (4) and (5), Eq. (1) can be recast in the form

$$\mathbf{u}(\mathbf{x}_1) = -\int_S \kappa(\mathbf{x}_2)\mathbf{J} \cdot \mathbf{n} d\sigma_2 + \kappa(\mathbf{x}_1)\int_{S'} \mathbf{J} \cdot \mathbf{n} d\sigma_2 + (\lambda - 1)\int_S [\mathbf{u}(\mathbf{x}_2) - \mathbf{u}(\mathbf{x}_1)] \cdot \mathbf{K} \cdot \mathbf{n} d\sigma_2 + \mathbf{u}^{(ext)}(\mathbf{x}_1), \tag{6}$$

where S' is an arbitrary closed surface. Equation (6) for the velocity on the surface S is the equation that forms the basis for all numerical calculations in this paper. Usually S' is taken to be the same as S, so as the integration variable $\mathbf{x}_2$ comes close to $\mathbf{x}_1$, the integrands become identical (up to a sign), and the singularity is subtracted. However, this procedure has to be modified for the present simulations, for which the curvature, appearing in the first integral, is very sharply peaked. This means that the second integral in Eq. (6) is multiplied by a large number (up to 10^9 in the case of our simulations), if $\mathbf{x}_1$ falls into a region of high curvature. As a result, tiny errors in the integral, stemming from contributions far away from the singular region, become hugely amplified.

A way around this problem is illustrated in Fig. 2. The second surface S' only agrees with S in a small cap region around the tip (the maximum curvature κ_m occurs on the z axis), whose size is of order $\kappa(\mathbf{x}_1)^{-1}$ and contains $\mathbf{x}_1$. Thus the contribution from the cap is small, yet S and S' are identical around the point of interest $\mathbf{x}_1$. The contribution coming from the cylindrical part of S' can be evaluated exactly in terms of elliptic integrals. The contribution from the far end of the cylinder goes to zero, so S' can be considered to be closed at infinity.

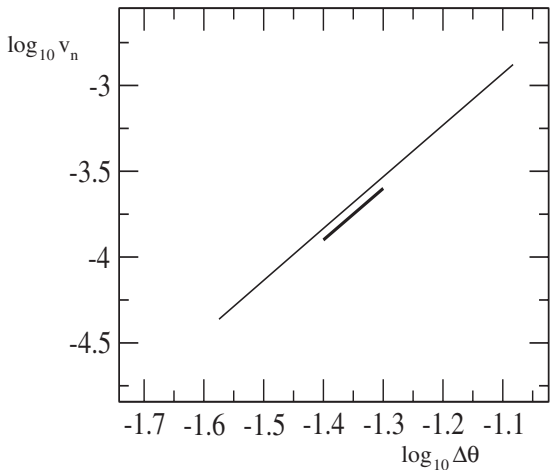

FIG. 3. The numerically determined *maximum* of the normal speed converges to zero like the third power of the grid spacing (given in terms of the polar angle θ). The fat line has a slope of −3.

Both integrals and derivatives are evaluated using the simplest possible finite-difference formulas based on polynomial interpolation. As the grid is highly graded to obtain sufficient resolution near the tip, all formulas are valid for unequally spaced grid points. The integration formula we used is of fourth order in the grid spacing, the formula for the second derivative (to compute the curvature κ) is of third order. Since the kernels of the integrals, after azimuthal integration, have logarithmic singularities, the kernel behaves like $x \ln x$ after the subtraction. This makes the error of the integral coming from a local region around the singularity of second order in the most unfavorable case of a nonuniform grid. If the grid around the singularity is uniform, the contribution from $x \ln x$ cancels and the method becomes third order. We choose the grid to vary gradually, so the second-order contribution to the error always remains small.

If k is the number of grid points needed to represent one quadrant of the drop, Eq. (6) is a matrix equation for $2k$ unknown velocity components (we only looked at situations symmetric with respect to $z \to -z$). This equation was solved using standard LU decomposition [30]. As a test of the numerical procedure to compute the velocity, we compared to an exactly solvable problem: the extensional flow around a spherical drop filled with an inviscid gas. Thus the external flow is

$$u_z^{(ext)} = Gz, \quad u_r^{(ext)} = -\frac{G}{2}r. \tag{7}$$

A calculation completely analogous to the *uniform* flow around a spherical drop [31] yields both the normal stress and the tangential velocity around the drop. Namely, for the normal stress we find

$$\boldsymbol{n} \cdot \boldsymbol{\sigma} \cdot \boldsymbol{n} = G[-4\sin(\theta)^2 + 8\cos(\theta)^2], \tag{8}$$

where θ is the polar angle. If this expression is inserted for κ into Eq. (6), the normal velocity v_n should be zero. This is seen in Fig. 3, which demonstrates the expected third-order convergence with grid spacing for a uniform grid.

The problems we are interested in exhibit a highly localized curvature at the tipped end of drops or at the centerline of the selective withdrawal experiment. The maximum of the curvature occurs on the centerline and then drops off rapidly as function of the polar angle θ. With this solution structure in mind, we determine the angle $\theta_{1/2}$ at which the curvature has fallen to half of its peak value. Based on this half-width, we use 50 grid points at constant grid spacing (as function of θ) up to $2\theta_{1/2}$ to resolve the central peak. After that, the grid spacing is increased geometrically, making sure the spacing does not change by more than 3% from one interval to the next, down to a maximum grid size, sufficient to resolve the $O(1)$ regions of the drop.

C. Newton's method

All results reported in this paper concern stationary solutions of the flow equations, i.e., solutions for which the normal velocity vanishes:

$$u^{(n)} = 0. \tag{9}$$

To compute $u^{(n)}$, one first has to solve Eq. (6) for the velocity itself and then multiply with the normal vector. The integrals over the surface of the drop can be reduced to integrals over the cross section by performing the azimuthal integration, and explicit expressions for the kernels are found in [26]. We solve for the shape of the drop, which we represented as the radius of the drop's cross section as function of the polar angle: $\rho=\rho(\theta)$. Thus there are k unknowns $\rho_i, i=1,\ldots,k$ at the node points and we demand $u^{(n)}$ to vanish at each of the nodes. To obtain a unique answer, one also needs to fix the volume V, so the condition $u_k^{(n)}=0$ at the equator of the drop was replaced by the requirement that volume is conserved. In units of the unperturbed radius, this implies that $V=4\pi/3$.

To implement Newton's method, the matrix

$$A_{ij} = \frac{\partial u_i^{(n)}}{\partial \rho_j} \tag{10}$$

is needed. As mentioned before, Eq. (6) can be written as a $2k$-dimensional matrix equation

$$M_{ij}(\{\rho_m\})v_j = f_i(\{\rho_m\}), \tag{11}$$

where $\{v_j\}$ is the vector of the node velocities. The partial derivatives become

$$\frac{\partial v_j}{\partial \rho_m} = M_{ij}^{-1}\left[\frac{\partial f_i}{\partial \rho_m} - \frac{\partial M_{il}}{\partial \rho_m}v_l\right]. \tag{12}$$

Note that to compute the derivatives, the LU decomposition only needs to be performed once, and then each equation can be solved by substitution, which is a $(2k)^2$ process [30]. Thus by carefully avoiding having to evaluate any of the derivatives twice, the whole process is of order $(2k)^3$.

Using definition (9), the derivatives A_{ij} of the normal velocities with respect to the ρ_j are easily computed. We then implemented Newton's method [30] in the most straightforward fashion. If one starts from a sufficiently good initial condition, we found the method to converge quadratically, as expected. The normal velocity $u^{(n)}$ always converged to values limited by numerical noise, coming from round-off errors. In the worst case, for a maximum local curvature of $\kappa_m \approx 10^9$, the maximum normal velocity was $\max(u^{(n)}) \approx 10^{-6}$. In addition, by computing the eigenvalues of the matrix A_{ij}, we can determine whether a given profile is stable: for this to be true, all eigenvalues must be negative.

D. Continuation

If one is searching for highly deformed drops, Newton's method will not converge starting from an equilibrium (spherical) drop. Instead, the shapes have to be continued using a parameter that measures the degree of deformation such as the strength of the flow G. Thus we initially search for the stationary state for a small value of G, which can be reached starting from an undeformed drop. Once a stationary profile has been found, we extrapolate along rays of constant θ_i to find a new initial value of ρ for each θ_i. To this end, we fit a polynomial to two or three consecutive pairs of values $[G,\rho(\theta_i)]$. The polynomial was then evaluated at a new value of G to obtain a starting profile for Newton's method.

To find the new value of G, we used a very simple "time stepping" procedure. Namely, a step was deemed successful if Newton's method converged to a certain error bound and if the maximum curvature of the resulting profile increased by no more than 20% from the last value. Otherwise the step was designated a failure and the step size was halved. Furthermore, if the initial residual of Newton's method was too large, the step was designated a failure from the outset. Using this method, we were generally able to continue the solution curve to maximum curvatures between 10^8 and 10^9. This typically took a few hours on a laptop computer. As a result, we obtained "solution curves" of one parameter, such as the drop length, as function of a control parameter such as the flow strength; see for example Fig. 6 below.

As we will discuss in more detail below, the curve of drop length as function of the flow strength is expected to continue forever if the interior of the drop is inviscid. If on the other hand the viscosity ratio λ is finite, solutions only continue up to a finite value G_c of the strength of the flow. Since the solution curve ends in a vertical tangent at this saddle-node bifurcation [17], it cannot be continued beyond this point and it is necessary to use another continuation parameter. One possibility is to use the major half-axis L of the drop and search for G as part of the solution. This permits to extend the solution beyond the bifurcation point and to obtain accurate values of G_c. Below we will also see that the drop shapes lose their stability precisely at the bifurcation point; i.e., the maximum eigenvalue goes to zero, consistent with a saddle-node bifurcation.

E. External flow

In the fundamental Eq. (6) of the boundary integral formulation, the external flow $\mathbf{u}^{(ext)}$ is driving the problem on a large scale. In the case of drops, a family of flows considered previously [22,23] is a generalization of Eq. (7):

$$u_z^{(ext)} = Gz(1+c_2z^2), \quad u_r^{(ext)} = -\frac{G}{2}r(1+3c_2z^2). \tag{13}$$

In particular, the purpose of the higher-order terms is to approximate the flow at the center of a "four roller" [1] appa-

ratus more accurately. For selective withdrawal, a realistic driving flow is a point source [see Eq. (30) below], as long as the radius of the pipe through which fluid is withdrawn is small compared to the distance from the horizontal interface. Quantitative comparison between experiment and simulation will provide ample evidence that this is indeed a realistic approximation. To realize the closest correspondence possible between the problem of a closed drop in an external flow and selective withdrawal, we also considered the case of a drop placed between two point sources of equal strength.

As we will explain in more detail in Sec. VI below, we found that the outer flow has very little impact on the local structure of tips once they are formed. For this reason, most of the results reported here refer to the simplest case of $c_2=0$, which well represents all scenarios which exhibit sharp tips. As pointed out in [23], for some flows there may exist no steady-state solution with tips, for example, if c_2 in Eq. (13) is sufficiently negative. We have confirmed this conclusion for the choice $c_2=-0.2/R^2$, in that we were not able to numerically continue to a pointed solution, starting from a spherical drop. However, our focus is on cases where tips do form, as it is overwhelmingly the case experimentally, if the flow is sufficiently strong.

III. DROPS

A. Drop shapes

Two different physical limits are amenable to theoretical analysis of drop deformation, but *excluding* the tip region [3,32]. First, the limit that the drop is close to spherical, or that the capillary number

$$\mathrm{Ca}=\frac{GR\eta}{\gamma} \tag{14}$$

is small. Below, we will use the unperturbed drop radius R to nondimensionalize all lengths. In this small deformation limit one may apply perturbation theory [33] in the capillary number. As seen in Fig. 4, our numerics are in excellent agreement with perturbation theory; however, perturbation theory rapidly becomes invalid if Ca is in the order of 0.2. The same result had previously been obtained by [28] and in unpublished work by Duffy and Blundell reported in [34]. On the other hand, the corresponding curve of D versus Ca for $c_2=0$, reported in [23], shows deformations about twice as great as ours, and thus appears to be inconsistent with perturbation theory. Our numerical solutions were obtained by starting from a small value of the capillary number, $\mathrm{Ca}\approx 0.01$, and gradually extending the solution as explained in the previous section.

Second, one can consider strongly deformed drops using the drop's slenderness ϵ as an expansion parameter [20]. Formally, this corresponds to the large capillary number limit, but Ca is always smaller than unity in practice. The large deformation theory, to be explained in some detail below, can be used to compute the shape of drops with vanishing and with finite but *small* viscosity ratio λ. In particular, the theory provides an explanation for the bursting of drops at some critical capillary number Ca_{cr}, which is a function of λ.

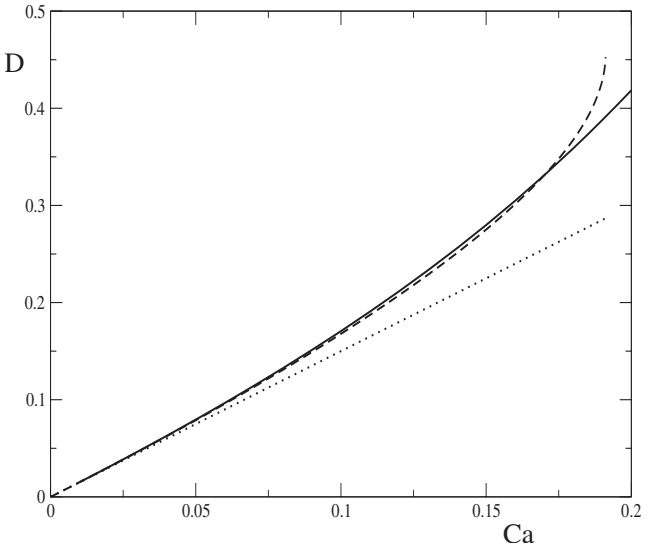

FIG. 4. The deformation $D=(\ell-b)/(\ell+b)$ of an inviscid ($\lambda=0$) drop (or gas bubble) as function of the capillary number. The major axis is ℓ; the minor axis is b. The full line is the result of the present numerical code, the dotted line perturbation theory to first order in Ca, and the dashed line second-order perturbation theory [33], which runs into a singularity.

For $\lambda=0$ the slender-body theory predicts a stationary drop for any value of Ca. In Fig. 5 we show as the solid line a numerically computed drop shape for the largest capillary number obtainable, for which $\kappa_m\approx 2.5\times 10^8$. Similar to the results at small deformation, drop shapes shown in [23] are far more elongated than ours at corresponding capillary numbers. Also, in all previous work no tests are reported confirming that the tip region remains fully resolved as the capillary number is increased.

The theory for the shape and stability of highly extended and slightly viscous drops was developed by Taylor and was communicated in a brief account [17]. Taylor's calculations were worked out in detail later using careful asymptotics [18–20], absent from his original account, but ultimately with identical results. The asymptotics is based on a systematic expansion in the aspect ratio (or slenderness) $\epsilon=b/\ell$ of the drop and viscosity ratios up to $\lambda=\epsilon^2$. Here the half-length of the drop is ℓ, its half-width b. Below we only give the intuitive version of the theory, based on the idea to treat the drop as a perturbation to the external flow, concentrated along the axis. This perturbation can be represented as a line distribution of 2D sources chosen to satisfy the boundary

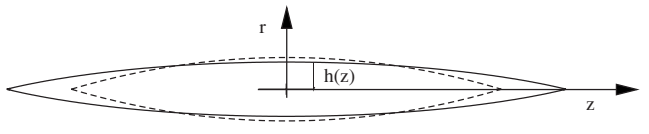

FIG. 5. The shape $h(z)$ of an inviscid ($\lambda=0$) drop (or bubble) at $\mathrm{Ca}=0.4393$, which is the highest capillary number presently achievable with our code. The curvature at the tip is $\kappa_m=2.54\times 10^8$. The dashed line is the prediction of Taylor's theory [Eqs. (18) and (19)]. The half-length of the drop (in units of R) is $l=4.797$, its half-width $b=0.497$, making the deformation parameter $D=0.812$.

conditions to leading order. This is indeed possible, and for any axisymmetric external flow leads to

$$\frac{dhu_z^{(ext)}}{dz} = h\frac{p(z)}{2} - \frac{1}{2}, \tag{15}$$

where $h(z)$ is the drop profile. The second member on the right is the contribution from surface tension; $p(z)$ is the pressure inside the drop. Near the end z_{end} of the drop, where h vanishes, the solution is a cone:

$$h = \frac{z_{end} - z}{2u_z^{(ext)}(z_{end})}, \tag{16}$$

whose opening angle depends on the local flow strength.

Description (15) breaks down at the very end of the drop (the tip), where the shape is no longer slender. Indeed, the conical solution (16) has been shown [18] to be inconsistent with the stationary flow equations. Nevertheless, one would still expect Eq. (15) to be the correct outer solution in the sense of matched asymptotic expansions [35]. The reason is that a solution of Eq. (15) is determined completely in terms of the requirement that h goes to zero at the tip, as well as the drop volume. Thus there is no free parameter to be fixed by the inner solution, which must rather adapt to the outer solution.

In the case of simple extensional flow (7), Eq. (15) reduces to

$$\mathrm{Ca}\frac{dhz}{dz} = h\frac{p(z)}{2} - \frac{1}{2}. \tag{17}$$

If in addition the viscosity of the drop fluid vanishes ($\lambda = 0$), the inner pressure is a constant: $p(z) = p_0$. It is simple to check that if the pressure is chosen to be $p_0 = 6\mathrm{Ca}$, a solution to Eq. (17), corresponding to a closed drop, becomes a simple quadratic:

$$h(z) = \frac{1}{4\mathrm{Ca}}\left[1 - \left(\frac{z}{\ell}\right)^2\right]. \tag{18}$$

Since the drop volume is $V = 4\pi/3$ in dimensionless variables, the drop half-length ℓ can be found from integrating Eq. (18):

$$\ell = 20\mathrm{Ca}^2. \tag{19}$$

It is argued in [20] that the quadratic solution (18) is the only *stable* solution of Eq. (17). The shape of the drop as given by Eqs. (18) and (19) is shown in Fig. 5 as the dashed line for a single capillary number. The numerical simulation gives a drop shape which is significantly more extended (full line). As an aside, the parabolic *shape*, with a properly adjusted value of ℓ, provides a very good (but of course not exact), fit for the shape of the drop. The inviscid prediction (19) for the Ca dependence of the drop length is compared to our simulations in Fig. 6. In spite of the drop being quite extended for the largest capillary number (the aspect ratio is about 10), the length is predicted only to within 30%. In particular, there is not yet a clear sign of the predicted quadratic growth in the length of the drop.

The above solution for an inviscid drop exists for all capillary numbers. In Taylor's theory a transition occurs only for

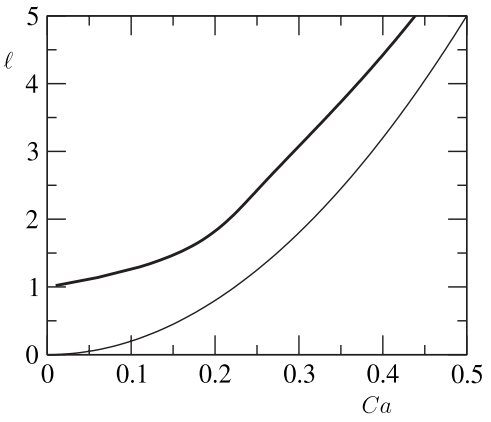

FIG. 6. The length of an inviscid drop ($\lambda = 0$) in an extensional flow as predicted by Taylor's theory: $\ell = 20\mathrm{Ca}^2$ (light line) and by the present simulations (heavy line).

finite λ, owing to the pressure building up near the ends of the drop, as we will see below. The pressure $p(z)$ in the interior of the drop can be evaluated using simple lubrication ideas [18,20], giving

$$p = p_0 + 8\lambda\mathrm{Ca}\int_0^z \frac{sds}{h^2(s)}. \tag{20}$$

The integration is along the axis of the drop. For $\lambda = 0$ the pressure is constant, which is the case considered previously. Inserting Eq. (20) into Eq. (17) and differentiating leads to a single differential equation for $h(z)$. It can be simplified using the similarity form

$$h(z) = \mathrm{Ca}^{-1}H(z/\ell), \tag{21}$$

where $\zeta = z/\ell$ is the axial coordinate, rescaled by the drop length. The result is

$$2(HH' + \zeta HH'' - \zeta H'^2) = 8\lambda\mathrm{Ca}^2\ell^2\zeta + H', \tag{22}$$

where the prime denotes differentiation with respect to the argument.

Equation (22) is to be solved with boundary conditions $H(\pm 1) = 0$, with the regular solution

$$H(\zeta) = A(1 - \zeta^2), \quad A = \frac{1}{8}[1 + \sqrt{1 - 64\lambda\mathrm{Ca}^2 l^2}]. \tag{23}$$

Once more, the drop length ℓ is determined by computing the volume, which is $V = 4\pi/3$ in units of R, giving

$$A = \sqrt{\frac{5}{4\ell}}\mathrm{Ca}. \tag{24}$$

Note that the drop shape is the same, whatever the value of λ, apart from a rescaling of the drop width and length. However, it is apparent from the form of the parameter A in Eq. (23), that the solution must break down with increasing λ. We study this bifurcation in the next subsection.

B. Drop bifurcation

The bifurcation of slightly viscous drop is caused by the lubrication pressure that builds up inside the drop. To find the

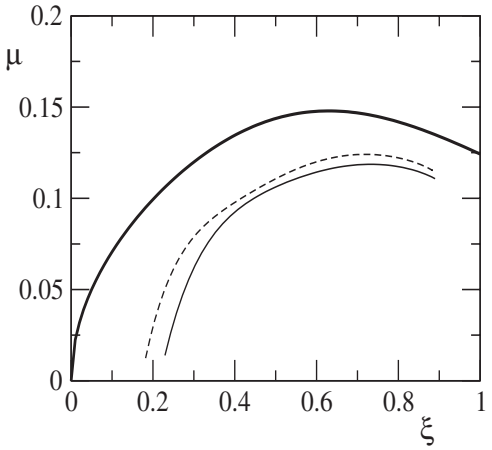

FIG. 7. The rescaled capillary parameter $\mu=\mathrm{Ca}\lambda^{1/6}$ plotted as function of the rescaled drop length $\xi=\ell\lambda^{1/3}$ for a drop with $\lambda=10^{-2}$ (full line) and $\lambda=5\times10^{-3}$ (dashed line). The heavy line is Taylor's universal theory [Eq. (25)]. The states to the left of the maximum are stable; the other side corresponds to unstable states.

bifurcation diagram, the parameter A is eliminated between Eqs. (23) and (24). The resulting equation is [17]

$$\mu=\frac{1}{\sqrt{20}}\frac{\sqrt{\xi}}{1+4\xi^3/5}, \tag{25}$$

where we have introduced the parameters

$$\mu=\mathrm{Ca}\lambda^{1/6}, \quad \xi=\ell\lambda^{1/3}. \tag{26}$$

The bifurcation curve, plotted in Fig. 7 as the heavy line, has the form of a saddle-node bifurcation [36]. At a critical value ξ_{cr} of the drop length, the capillary parameter reaches a *maximum* value μ_{cr}. From Eq. (25), the numerical values are

$$\mu_{cr}=\frac{5^{1/2}2^{2/3}}{24}, \quad \xi_{cr}=2^{-2/3}. \tag{27}$$

Thus, in terms of the control parameter, the solution vanishes if Ca is greater than a critical value

$$\mathrm{Ca}_{cr}=\frac{5^{1/2}2^{2/3}}{24}\lambda^{-1/6}. \tag{28}$$

The form of the bifurcation curve (25) was tested in Fig. 7 for two different values of λ. In agreement with slender-body theory [see Eq. (23) above], we find the drop shapes for finite λ to be virtually indistinguishable from their inviscid counterpart shown in Fig. 5. To be able to go across the bifurcation point, the flow strength G was held constant, but the length of the drop ℓ is stepped up. For each Newton search, $\rho(0)=\ell$ is held constant, and the $\rho_i, i=2,\ldots,k$ are sought. Thus instead of the drop volume being a constraint, it now comes out as part of the solution, which determines R. With this value of R we can determine Ca and nondimensionalize ℓ to compute the parameters μ and ξ according to Eq. (26). As a result, we obtain the full and dashed curves in Fig. 7. Both curves exhibit a maximum, in line with Taylor's theory. In the limit of infinite slenderness, all results are expected to collapse onto the heavy line. Indeed, for smaller λ the numerical curve is closer to the theoretical result. However, although the drops are reasonably slender (the maximum slenderness is $\epsilon=b/\ell=0.09$), there remain considerable quantitative differences. We have also performed a linear stability analysis around each stationary shape to be described in more detail in the next section for the case of selective withdrawal. As expected for a saddle-node bifurcation, all solutions to the left of ξ_{cr} are stable, the others are unstable, meaning that the largest eigenvalue of the matrix A_{ij} in Eq. (10) goes through zero at ξ_{cr}.

Result (28) for the upper critical capillary number is tested separately in Fig. 8 (left). To allow for a more quantitative comparison, C_{cr} was multiplied by $\lambda^{1/6}$, so Taylor's theory predicts a horizontal line. The numerical data are consistent with a logarithmic dependence of the prefactor on λ, which is not captured by the theory. Since the tip region has been neglected in the theoretical description, Eq. (28) is strictly speaking only an upper bound, since other instabilities might be triggered by *localized* perturbations in the tip region. However, this scenario is not likely considering the eigenfunction of the mode which turns unstable at the bifurcation: it remains relatively smooth on the scale set by the inverse curvature.

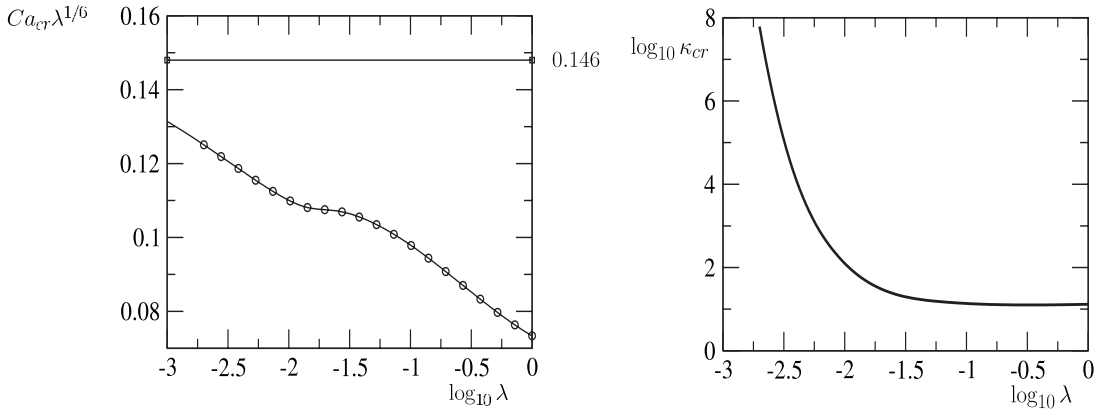

FIG. 8. A comparison between Taylor's theory for the instability of a slightly viscous drop and the present numerical simulations is shown on the left. The horizontal line at $\mathrm{Ca}_{cr}\lambda^{1/6}=0.146$ represents Taylor's theory. On the right, we show the value of the tip curvature reached at the point of instability.

To understand the mechanism leading to the bursting of drops, it is instructive to compute the pressure in the interior. Inserting solution (23) into Eq. (17) one finds

$$p(\zeta) = p_0 + \frac{16}{5}\lambda \ell^3 \mathrm{Ca} \frac{\zeta^2}{1-\zeta^2}, \quad p_0 = \mathrm{Ca}\left(\frac{2\sqrt{\ell}}{\sqrt{5}\mathrm{Ca}} + 2\right). \tag{29}$$

Note that pressure (29) diverges at the tip $\zeta = z/\ell = 1$, as does the Laplace pressure near a conical tip. This is a reflection of the fact that the slender-body solution breaks down at the tip and will have to be replaced by another, local solution. In the limit $\lambda = 0$ one recovers the previous inviscid result.

The pressure that builds up near the end of the drop diverges like $p \propto \lambda \mathrm{Ca} \ell^3/(1-\zeta^2)$, while the capillary pressure behaves like $p_{cap} \propto 1/h \propto \mathrm{Ca}/H \propto \mathrm{Ca}/(1-\zeta^2)$. For the drop to be unstable the two must be of the same order, which implies $\lambda \ell^3 \propto \lambda \mathrm{Ca}^6 = O(1)$, using $\ell \propto \mathrm{Ca}^2$. This explains the scaling of the critical capillary number found in Eq. (28). The mechanism for the instability has been described in [21]: the increased inner pressure pushes the drop ends outward, increasing the length ℓ of the drop, which on account of volume conservation means that the drop has to become *narrower*. But this means the interior lubrication pressure has to increase even more, thus promoting instability. Note that the pressure p_0 in the center of the drop is subdominant relative to the pressure that builds up near the end (p_0 does however increase with Ca owing to increasing squeezing by the outer flow). Thus we can conclude that the volume constraint plays an insignificant role in producing instability. In particular, a similar mechanism is expected to be at work for the selective withdrawal geometry.

The instability mechanism described above is quite similar to that responsible for the breaking of a *two-dimensional* cusp, first described in [37]. However, a crucial difference is that in the two-dimensional case the pressure builds up entirely inside the self-similar tip region. First, this makes the criterion for the bursting of a cusp universal, independent of the large scale geometry. Second, in the two-dimensional case the instability is directly related to the curvature of the cusp limiting the maximum curvature that can be reached. In the present three-dimensional case, the tip curvature can reach much higher values without affecting stability, as shown in Fig. 8 (right). The value of the tip curvature is described essentially by the case of an inviscid drop ($\lambda = 0$), to be discussed in more detail in Sec. VI below. In the next section, we will see that the criterion for the bifurcation is different for the two geometries considered in this paper. Thus the bifurcation of a three-dimensional tip is indeed less universal than its two-dimensional counterpart.

IV. SELECTIVE WITHDRAWAL

A. Basic properties

Next we consider the selective withdrawal geometry, cf. Fig. 9; see also the experimental picture in Fig. 1 [2]. In an experiment with two liquids, lighter liquid is withdrawn from above heavy liquid [6], while in Fig. 1 the situation is reversed: fluid escapes from below an air atmosphere through a

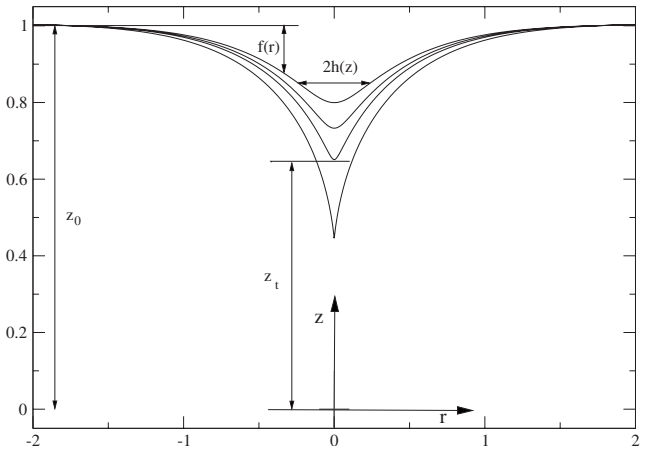

FIG. 9. Computed interface profiles for selective withdrawal, over a wide range of tip curvatures, in units of the distance z_0 between the sink and the unperturbed interface. The position of the sink is also taken as origin of the coordinate system. The distance between the tip and the sink is denoted z_t. The second parameter of Eq. (32) is $\Gamma = 1/9$, the dimensionless flow strength takes the values $Q = 0.36$, 0.42, 0.474, and 0.6066. For the latter value, the tip curvature reaches 2.9×10^8.

sink hole. In our simulations, we treat the fluid as being of infinite extent, both vertically and horizontally. A point sink of strength q is placed at the origin of the coordinate system:

$$\mathbf{u}^{(ext)} = -\frac{q}{4\pi}\frac{\mathbf{r}}{|\mathbf{r}|^3}, \tag{30}$$

which is at a distance z_0 from the equilibrium surface. The viscosity of the fluid that is being withdrawn is η, that of the other fluid (or gas) is $\lambda\eta$. The surface is most conveniently represented as the height $f(r)$ above the equilibrium value and where r is the radial distance from the centerline (cf. Fig. 9). Hydrostatic pressure is included by introducing the inviscid part of the pressure jump as $\Delta p = \gamma\kappa - \Delta\rho g f(r)$ across the interface, where $\Delta\rho$ is the density contrast and g is the acceleration of gravity [38].

Using the capillary length $\ell_c = \sqrt{\gamma/(\Delta\rho g)}$ as a length scale and the corresponding time scale $\eta\ell_c/\gamma$ to nondimensionalize the equations, the problem is controlled by the two parameters

$$\chi = \frac{q\eta}{\ell_c^2 \gamma}, \quad E = \frac{z_0}{\ell_c}. \tag{31}$$

Alternatively, one can use the parameters introduced in [38]:

$$Q = \frac{q\eta}{\Delta\rho g z_0^4} \equiv \frac{\chi}{E^4}, \quad \Gamma = \frac{\gamma}{\Delta\rho g z_0^2} \equiv \frac{1}{E^2}, \tag{32}$$

which correspond to using z_0 as a length scale and $\eta/(\rho g z_0)$ as the time scale.

Lister [38] developed a perturbation theory in the sink strength Q for the case $\lambda = 1$, but which is easily generalized to arbitrary λ, using the solutions given in [39]. Surprisingly, the leading order equation for the interface turns out to be *independent* of λ, so the general result is the same as the one found in [38]:

$$f(r) - \Gamma\left(f'' + \frac{f'}{r}\right) = \frac{Q}{\pi}\frac{2 - r^2}{(1 + r^2)^{5/2}}n. \tag{33}$$

For large distances r from the center this leads to the universal behavior

$$f(r) \approx -\frac{Q}{\pi r^3}, \tag{34}$$

hence far away from the sink (compared to the capillary length), the interface shape is controlled by a balance of viscous forces and gravity. Interestingly, the surface is lifted *up* far away from the line of symmetry rather than being pulled down by the sink. We also rederived Lister's theory for the next order, at which the result becomes λ dependent. We used the result as a check of our fully nonlinear numerics, but there is no need to present it here, since the calculation is very similar to the $\lambda = 1$ case.

The interface between the two phases is not closed, so Eq. (1) cannot be applied directly. We closed the interface using a cylindrical box S_∞, whose radius and height are sent to infinity. The J integral on the right of Eq. (1) does not give a contribution from S_∞, while the K integral is calculated as

$$\int_{S_\infty} \mathbf{u} \cdot \mathbf{K} \cdot \mathbf{n} d\sigma = \frac{1}{2}\mathbf{u}, \tag{35}$$

the contribution of which is included when evaluating Eq. (6). To perform the indefinite integral over the *horizontal* surface extending to infinity, grid points are chosen at regularly spaced intervals in the polar angle θ. At the point $\theta = \pi/2$ at infinity, the deformation and the curvature are zero. Numerical results are in excellent agreement with the theoretical prediction (34). In an alternative version of the code, the elevation of the surface and its curvature was held fixed at the value prescribed by Eq. (34) at the last grid point. Both methods give answers virtually indistinguishable from each other, but the latter version is slightly more accurate. It brings down the numerical error in computing the far-field curvature to about 10^{-8}. Typical profiles, computed using the above a procedure, are shown in Fig. 9. Only the center region near the hump is shown (the last grid point is at $r = 200$). We now continue with a more detailed study of the transition from the hump toward a jet, which is also referred to as a "spout" [5].

B. Bifurcation

The structure of the bifurcation observed for selective withdrawal is very similar to that observed for drops as shown in Fig. 10. In complete analogy to Fig. 7, the flow strength Q goes through a maximum as function of the height of the hump $f(0)$. Interestingly, the bifurcation curve continues to oscillate beyond the bifurcation point, a feature reminiscent of liquid film transitions with receding contact lines [40]. The corresponding real-space profiles are shown in Fig. 11. No obvious feature distinguishes profiles just above and below the transition. However, as $f(0)$ is raised to a value far above the transition, the profile becomes much more pointed. A closeup (inset) reveals a sharp nose that is

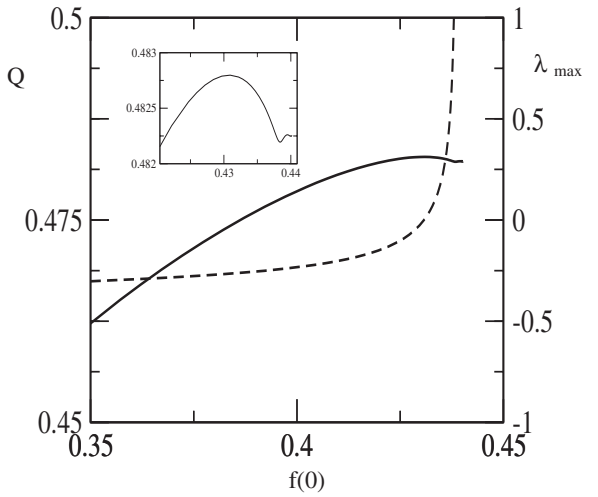

FIG. 10. A bifurcation diagram for $\lambda = 0.1$ and $\Gamma = 1/\sqrt{3}$. The full line is the source strength Q; the dashed line the maximum eigenvalue λ_{max}. The inset shows a detail of the bifurcation curve, which oscillates beyond the bifurcation point.

reminiscent of thin jets observed experimentally [41]. This profile is indicative of structures that may form dynamically above the transition.

The dynamical equation governing the motion of the interface profile $f(r,t)$ is

$$\partial_t f = \sqrt{1 + (\partial_r f)^2}u^{(n)}, \tag{36}$$

where the normal velocity $u^{(n)}$ is computed according to Eq. (9). Thus if one of the eigenvalues of the matrix A_{ij} [see Eq. (10)] is positive, the profile is unstable. The dashed line of Fig. 10 shows the largest eigenvalue λ_{max} of A_{ij}. At the bifurcation point (first maximum of the full line) λ_{max} goes through zero, as expected for a saddle-node bifurcation [25,36]. The final profile, showing the birth of a hump (inset

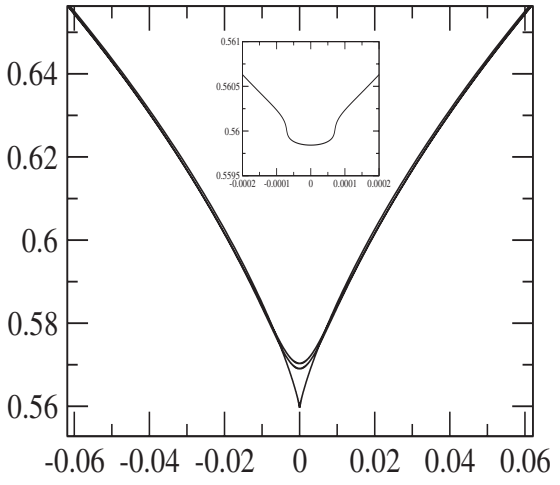

FIG. 11. Interface profiles corresponding to Fig. 10. The upper two profiles are just below or above the transition, $Q = 0.4828$; the bottom profile is at $Q = 0.4822$, far above the transition, $\lambda_{max} = 40$. The inset shows a closeup of the tip of the bottom profile.

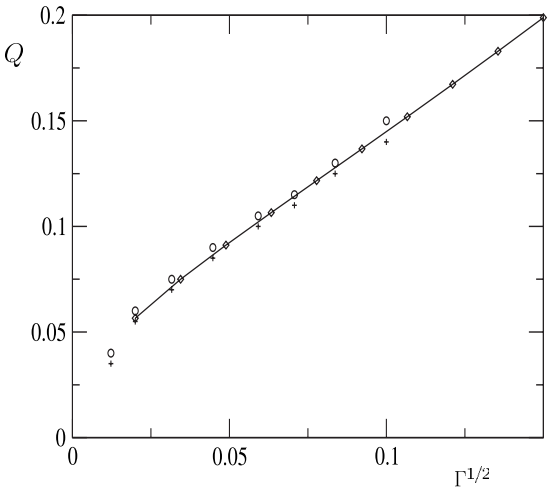

FIG. 12. The stability boundary for $\lambda=1$. Crosses and circles mark upper and lower bounds as given in [38]. Diamonds are the result of the present numerical code; the line is a guide for the eyes.

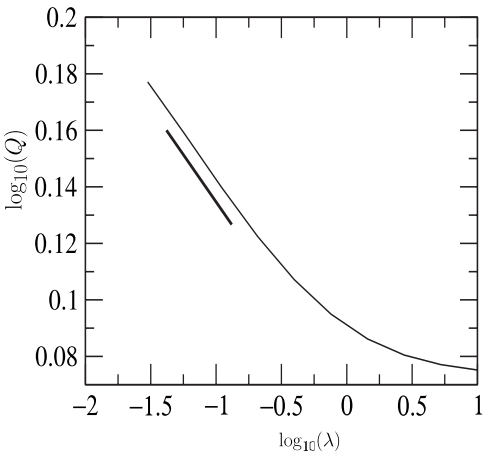

FIG. 13. Critical values of the flow strength Q as function of λ, at a fixed value of $\Gamma=1/\sqrt{3}$. The slope shown is 1/15.

of Fig. 11), corresponds to a large positive eigenvalue and is therefore quite unstable.

As a test, we compare to the earlier results of [38] for the case $\lambda=1$. To that end, as for the rest of this section, we will be using the dimensionless parameters (32) of Lister. As the effective flow rate Q is increased, the lower fluid rises up to form a hump [6]. If the value is raised above a critical value, the profile becomes unstable and a jet is formed. As seen in Fig. 12, the critical value increases with the surface tension parameter Γ. In [38] the boundary was determined using a dynamical code: the lower estimate corresponds to the largest Q for which a stationary profile could be observed; the upper estimate corresponds to dynamical solutions.

With the present code, the bifurcation point was determined as for the drop case. Namely, the height $f_0 \equiv f(0)$ of the hump was held constant and the corresponding value of Q was sought. The local maximum value of Q corresponds to the bifurcation point marked by diamonds in Fig. 12. As apparent from the figure, the agreement with the earlier dynamical simulations is excellent.

Finally, we monitor the flow strength at which instability occurs, in analogy to Fig. 8 in the case of drops. For small λ, the relationship between the critical flow strength seems to be well described by a power law, with slope 1/15, see Fig. 13. Even if one allows for the fact that the effective capillary number at the tip scales roughly like $\mathrm{Ca} \propto Q^{1/2}$, this is still a somewhat weaker dependence than that for drops.

V. COMPARISON TO EXPERIMENT

A. Scaling of the tip

Previous experimental work [2,5,6] was motivated largely by the question of whether there exists a singularity of the curvature at finite capillary number. A singularity would imply the formation of arbitrarily small free-surface features even at finite driving. Our numerical simulations reproduce previous experimental data and the scaling descriptions found over a finite range of curvatures. However, if we follow the data to higher curvatures than was considered previously, we find the scaling laws to fail. Instead, in the next section we will present numerical evidence that a singularity does not exist, but that the tip remains rounded at finite driving.

The most detailed recent study of the selective withdrawal geometry using two different fluids was reported in [5,6], withdrawing a less dense fluid from above another fluid through a pipette. The viscosity ratio is typically between $\lambda \approx 1$ and 10^{-3}, but more recently the reverse case of $\lambda \approx 20$ was considered as well [41]. The fluids reside in a large tank, hence the extent of the interface can be considered infinite to a good approximation. Experiments were performed at a constant distance z_0 between the pipette and the equilibrium interface position, while the flow rate was varied. Below we simulate the two-fluid selective withdrawal experiment using an experimental pipette height $z_0 = 0.921$ cm for reference, much larger than the pipette diameter of $D=0.16$ cm. Thus we expect our approximation of a point sink for the pipette to be appropriate.

In [5,6], scaling behavior was found when plotting the tip curvature as function of the maximum height $f(0)$ of the surface deformation:

$$\kappa_m = A\left(\frac{f_0^c - f_0}{f_0}\right)^{\alpha}, \quad \alpha = -1.163. \tag{37}$$

Note the nonstandard combination $(f_0^c - f_0)/f_0$ in the dependence on the hump height chosen by [5]. Over a limited range to the right of the arrow in Fig. 14, our simulations give agreement similar to that found in [5]. Using three adjustable parameters, the maximum range over which Eq. (37) is an acceptable description was about two decades. However at higher flow rates the simulated curvature falls below the expected power law. The failure of the scaling law (37) was not seen in experiment, since the curve was cut off by a transition toward a jet [6].

Next we turn to the comparison to recent experiments using a fluid-air system described in more detail in [2]. The experimental flow is generated by a sink hole of 1 mm diameter inside a container 3 cm wide. The most important

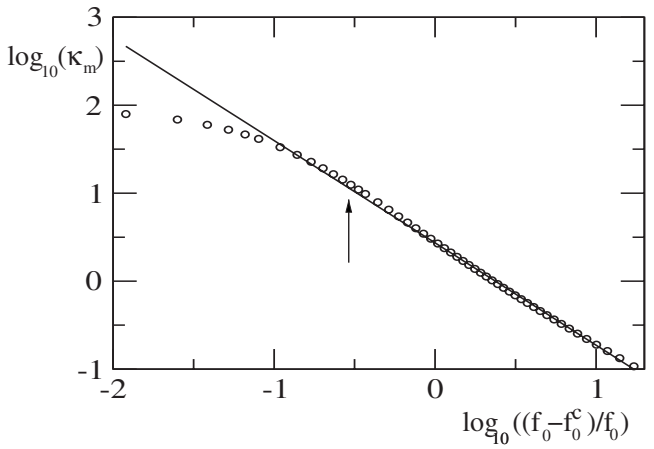

FIG. 14. A numerical computation of the tip curvature varying the flow rate. Parameters correspond to system 5 of [6] and $z_0=0.921$ cm. This gives the dimensionless parameters $E=1.354$ and $\lambda=5.9\times10^{-3}$. Lengths are given in units of the capillary length. The tip curvature data are fitted to Eq. (37) over the range shown to the right of the arrow, giving $A=2.726$, $f_0^c=0.6606$, and $\alpha=-1.184$.

difference in the experimental protocol as compared to [5] is that for a given sequence of profiles, the flow rate is kept constant, and the distance between the sink hole and the free surface is changed adiabatically. It is difficult to recreate this experimental geometry exactly. Instead, we chose a conceptually simple setup that is reasonably close to the real situation. Namely, we simulate the same flow as described in Sec. IV, but instead of the isotropic sink flow (30) choose

$$\mathbf{u}^{(ext)} = -\frac{3q}{2\pi}\frac{\mathbf{r}}{|\mathbf{r}|^3}\cos^2\theta, \tag{38}$$

where θ is the polar angle. The flow (38) is the Stokes flow of a point hole in an infinitely extended flat plate [31]. This means we ignore the coupling between the free surface and the bottom of the experimental cell. To model a solid plate correctly, it would have been necessary to replace Green's function (2) with the Green's function appropriate for half space. We will now demonstrate that in spite of these simplifications, excellent agreement with experiment is found for the tip region. This is sufficient, as our focus is really on the universal properties close to the tip.

In Fig. 15, we compare the numerically computed tip curvature to experiment, for a given flow rate q and fluid viscosity η. It is obvious that using the computation, a far greater range of curvatures can be explored. All the available experimental data fits the numerical results very well. The distance z_t of the tip from the sink hole in the numerical data has been shifted by a distance of 0.075 mm, less than 10% of the experimental hole diameter. The necessity of a small shift is of course to be expected, since the sink hole is not ideally small.

In [2], it is found that at a given flow rate, the tip curvature κ_m is controlled by the distance z_t between the tip and sink hole. More importantly, the experimental evidence suggests that the size of the tip *vanishes* at a finite distance z_t^*.

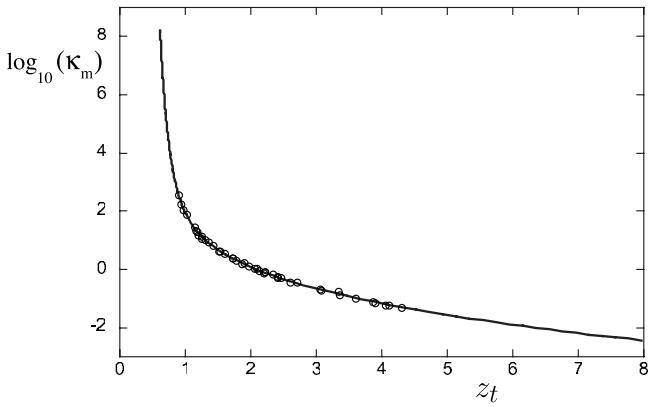

FIG. 15. The tip curvature as function of the distance z_t between the tip and the nozzle; lengths are in units of the capillary length $\ell_c=1.491$ mm. The flow rate is $q=1.32\times10^{-9}$ m^3/s and $\eta=60$ Pa s, and hence $\chi=1.7763$. Note that the curvature reported in [2] is the one-dimensional curvature, half the value of κ. The full line is our computation; z_t has been shifted by 0.05 to the right. Symbols ◇ and ◯ correspond to two different experimental runs.

All the available experimental data, for a variety of flow rates, could be summarized by the single law

$$\kappa_m = 2.16\frac{\chi^{1/2}}{(z_t - z_t^\star)^3}. \tag{39}$$

As is seen in Fig. 16, there seems to be equally good agreement with Eq. (39), over more than three decades in curvature up to $\kappa_m\ell_c \approx 10^3$, all being reported in units of ℓ_c. The numerical prefactor also is in good agreement with experiment. Unfortunately, this agreement does not persist if data is considered beyond κ_m values accessible experimentally, as seen in Fig. 16. In fact, for the presumably singular value $z_t=z_t^*$ the numerics still gives a finite curvature of $\kappa_m=20.2$ μm^{-1}, and the simulation is eventually continued up to $\kappa_m=1.54\times10^5$ μm^{-1}, at $z_t=1.746$ mm. In the next sec-

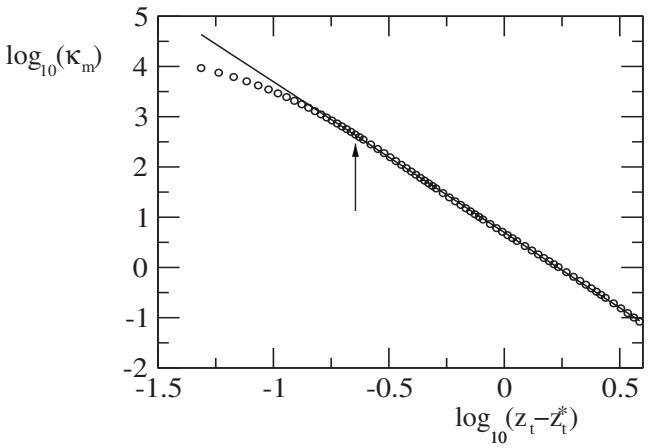

FIG. 16. A numerical computation of the tip curvature as function of the distance z_t, for $\chi=6.3312$. All lengths are in units of ℓ_c. The full line is the fit $\kappa_m=4.964/(z_t-z_t^*)^3$, and $z_t^*=1.388$. The fit parameters were determined using the data up to the position of the arrow. The experimental prediction for the prefactor is 5.43.

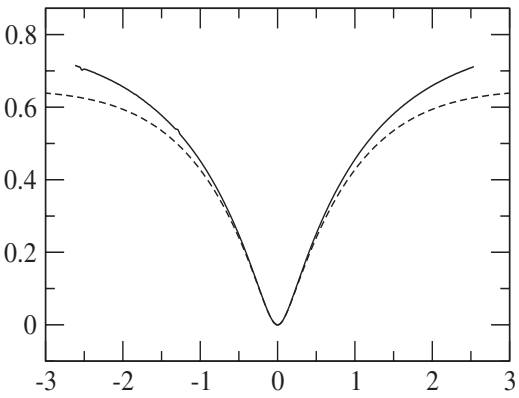

FIG. 17. The tip profile at $\kappa_m=5.607$; the full line is experiment, the dashed line simulation. Parameters are as in Fig. 15. In the simulation, z_t has been chosen to match the experimental curvature.

tion we will see that numerics suggests a (super)exponential law, which predicts rapid growth of the curvature; however, the curvature never goes infinite.

B. Experimental profiles

We now turn to the analysis of the entire profile, which has not been much studied. First we compare an entire experimental profile to simulation as seen in Fig. 17; the corresponding value of $h=1.27\ell_c$ can be found from Fig. 15. The neighborhood of the tip is described very well. This explains the excellent theoretical prediction of the tip curvature, which depends on local flow properties; also see Sec. VI below. Farther away, however, significant differences appear. This is to be expected, since away from the tip we have essentially a thin film flow over a solid boundary (the bottom of the container). As explained above, our present code is in fact ignoring the effect of the solid boundary on the free interface. Another factor might be the finite lateral size of the experimental cell.

Analysis of the experimental profiles at constant q has led us to a remarkable relation between different profiles, which can be summarized by the following law, valid away from the tip:

$$F(r) = z_0 - f[r - \Delta r(z_t)] - \Delta z(z_t). \tag{40}$$

As shown in Fig. 18, one side of each profile can be superimposed onto a master curve $F(r)$, if shifted by an appropriate value $\Delta z(z_t)$ and $\Delta r(z_t)$ in the z and r directions, respectively. Evidently, this invariance cannot work at the tip itself and is thus most significant when the tip is very small. We do not have a theoretical explanation for Eq. (40), but it provides us with a means of making contact with Taylor's slender-body theory (15). The convention adopted in Eq. (40) is such that $F(r)$ is the position of the interface measured from the sink upward (cf. Fig. 9). In particular, in the limit of vanishing z_t, Δr and Δz must go to zero, so $F(r)$ is simply the profile in the limit that the tip reaches the sink.

In the limit of vanishing viscosity of the air, the pressure $p(z)$ in Eq. (15) is constant, and in fact zero since the profile, unlike a drop, is not closed. Thus integrating Eq. (15) once, one obtains

$$hu^{(ext)} = -z/2, \tag{41}$$

valid close to the tip where the profile is slender and where hydrostatic pressure is negligible. Thus using the external flow (38), we arrive at a prediction for the interface profile near the sink hole, which does not contain any free parameters:

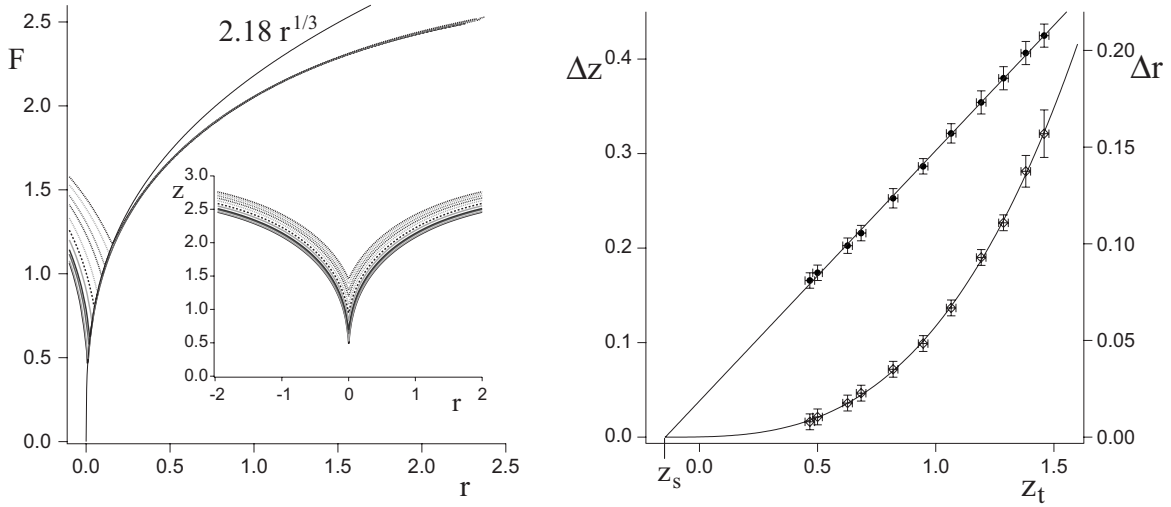

FIG. 18. The experimental interface profiles can be superimposed according to Eq. (40) onto a master curve as shown on the left. The inset shows the original unshifted profiles. The experimental parameters are $q=9.97\times10^{-9}$ m^3/s, $\eta=30$ Pa s, $\gamma=2.13\times10^{-2}$ N/m, and $\rho=976$ kg/m^3. The values of the necessary shifts $\Delta z(z_t)$ (closed symbols) and $\Delta r(z_t)$ (open symbols) are shown on the right. The shifts are fitted to Eq. (43), allowing for a sink that is by $z_s=0.144$ below its physical position. The fit gives $a=0.265$ and $b=0.0383$. The master curve is fitted to $F(r)=Ar^{1/3}$, with $A=(1-a)/b^{1/3}=2.18$.

$$F(r) = \left(\frac{3\chi}{\pi}\right)^{1/3} r^{1/3}. \tag{42}$$

Here all lengths are measured in units of the capillary length and χ is defined by Eq. (31). The prediction (42) is in good agreement with experiment, where a best fit of the form $F(r)=Ar^{1/3}$ gives a prefactor of $A=2.18$, whereas Eq. (42) yields $A=1.82$.

Once the power-law behavior of $F(r)$ is known, one can also gain information on the shifts Δz and Δr. By setting $r=\Delta r$ in Eq. (40) one finds that $F(\Delta r)=z_0-f(0)-\Delta z=z_t-\Delta z$. First, it is to be expected that Δz is a regular function of z_t, since it is measured relative to the position of the planar interface, which represents the far-field behavior of the problem. Thus one expects a linear dependence, as in Eq. (43) below; this automatically fixes Δr in terms of F and Eq. (42) yields the following power laws:

$$\Delta z = a z_t, \quad \Delta r = b z_t^3. \tag{43}$$

The prefactors a,b are related to the prefactor of $F(r)$ by $A=(1-a)/b^{1/3}$. In Fig. 18, we used this relationship to constrain the fits: first, we determined a and b from a fit to Eq. (43), as shown in Fig. 18, right. The value of $A=2.18$ obtained from a,b is shown in the comparison to $F(r)$ on the left. We have confirmed that the shift invariance (40) is valid for the numerically computed profiles as well, as expected. However, the available numerical data extend only to much smaller capillary number and therefore yields much less significant comparisons.

C. Jet transition

Finally, we turn to the stability of the interface and its transition toward a jetting state. In the two-fluid experiments [5,6], the hump turned into a jet at about $\kappa_m \ell_c \approx 15$, more or less *independent* of the value of λ between 10^{-3} and 2. In our simulations, we observe a transition at similar values of κ_m if λ is of order unity. For example, for $\lambda=1.26$ (system 4, see [6]) we find a maximum curvature of $15.3\ell_c^{-1}$, while [6] find $14\pm 6\ell_c^{-1}$. However, as implied by the discussion of the previous section (cf. Fig. 13), the simulations predict a very rapid rise of the tip curvature at the transition with decreasing λ. Indeed, for $\lambda=5.9\times10^{-3}$, realized for system 5 of [6] (cf. Fig. 14), we no longer found any evidence of a transition, even for the largest curvatures we are able to resolve. Thus there is a qualitative disagreement between our numerical simulations of Stokes flow and experimental observation in the two-fluid experiment. Experiments with an air-fluid interface, for which λ is between 2×10^{-5} and 3×10^{-7} [2], on the other hand, show no signs of a transition, whatever the flow rate. This observation is in line with simulations. We have no explanation for this qualitative difference between the two experiments.

VI. UNIVERSALITY

We have seen in Sec. III B that the stability of the tip is controlled by the pressure that accumulates over the conical part of the drop (or hump in the withdrawal case), see Eq. (29) in particular. It is quite independent of the tip itself, which can become extremely sharp even at moderate flow strengths, as shown in Fig. 8. In particular, for typical drop sizes ($R\approx 1$ mm) the curvature at the point of instability of the less viscous drops corresponds to subatomic radii of curvature at the tip. It is thus clear that at least in practice the transition cannot be controlled by the tip size. This is in line with Taylor's theory of Sec. III, which assumes the tip size to be zero (apart from the fact that structures of this size would not be describable by continuum theory).

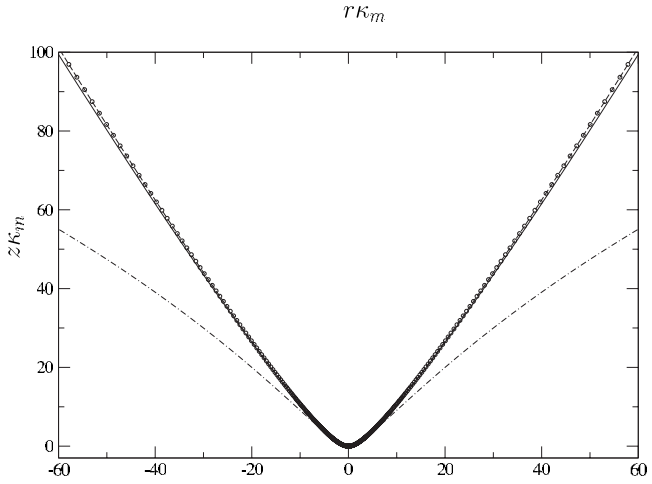

FIG. 19. The tip rescaled by the tip curvature. The full line and dot-dashed lines correspond to selective withdrawal at $\kappa_m=2.9\times10^8$ and $\kappa_m=10^6$. The dashed line is for a drop in extensional flow at $\kappa_m=2.6\times10^8$; the symbols are for the same drop, but $\kappa_m=2\times10^6$. The profiles, although generated by very different flows, collapse onto a universal function ϕ, as suggested by Eq. (44). The curve at a much smaller curvature demonstrates the slowness of the approach to a universal law for selective withdrawal. The two curves for a drop, on the other hand, are indistinguishable.

Having established that the transition toward a jet and the shape of the tip are quite separate issues, let us focus on the properties of the tip in the limiting case $\lambda=0$ for the remainder of this section. We will show that the behavior of the tip is universal, i.e., independent of the outer flow and of the gross geometry (selective withdrawal or single drop case). We begin with a discussion of the axisymmetric shape $h(z)$ near the tip, where $h(z)$ is defined in analogy to the drop profile; see Fig. 9. In the slender-body theory of Sec. III this shape was singular at the tip, corresponding to infinite curvature. For finite but large curvature, one expects a similarity solution of the form [11,37]

$$h(z) = \kappa_m^{-1} \phi[(z - z_{tip})\kappa_m], \tag{44}$$

where ϕ is a universal function, independent of the outer flow geometry. This is indeed the case as seen in Fig. 19. The approach to the scaling function ϕ is however much quicker in the case of a drop, owing to the fact that its shape is entirely convex. As a result, the two rescaled drop tips, for curvatures more than 2 orders of magnitude apart, are virtually indistinguishable. The same remains true if one subjects a drop to very different flow fields, such as the extensional flow (7), its nonlinear version [Eq. (13)], or the sink flow

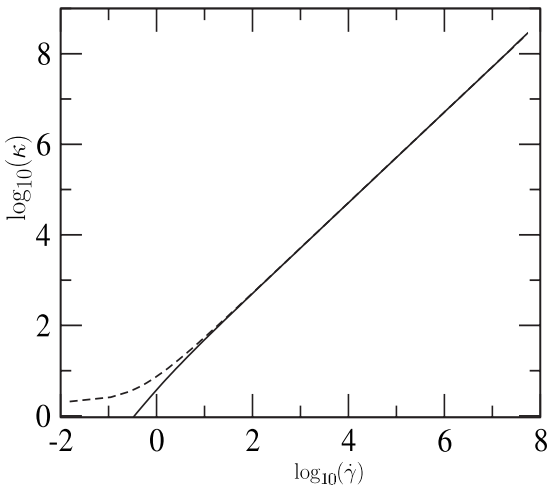

FIG. 20. The curvature as function of the extension rate $\dot{\gamma}$ at the tip for both a drop in extensional flow (solid line) and for selective withdrawal (dashed line), $\lambda=0$. For large curvature, both curves are in very close agreement with $\kappa_m=\frac{5.13\eta}{\gamma}\dot{\gamma}$.

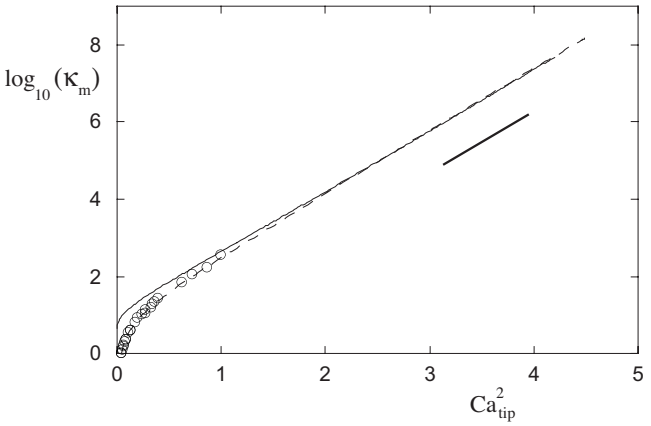

FIG. 21. The tip curvature as function of the square of the capillary number Ca_{tip} based on the *unperturbed* velocity (7) at the tip. The solid line is for an inviscid drop in an extensional flow, the dashed line for selective withdrawal, $\chi=1.7763$; the symbols are from the corresponding experiment. The heavy line has a slope of $a=1.6$. We have rescaled the curvature of the drop by an arbitrary constant to make the asymptotic behavior collapse.

(30). Of course this statement is contingent on the fact that a tip actually forms; as shown in [23], there are some flow fields [Eq. (13)] with c_2 negative where the drop appears to burst before a tip occurs.

At the highest curvature, the rescaled tip profile in the selective withdrawal geometry superimposes very well with the drop profile, but at a lower curvature collapse only occurs close to the tip. This illustrates the slow approach to the asymptotic limit for selective withdrawal, most likely due to the fact that the curvature changes sign away from the tip. As yet there is no explanation for the shape of the tip itself. A considerable technical problem is that the tip is not slender, so Eq. (17) is not valid.

Since the shape of the tip region is universal according to Eq. (44), the same can expected for the flow close to the tip. In that case dimensional analysis implies that there is a linear relationship between the tip curvature and the extension rate $\dot{\gamma}\equiv\partial v_r/\partial r$ at the tip; from incompressibility, one also has $\dot{\gamma}=-\partial v_z/\partial z$. Note that the extension rate is computed on the basis of the *full* velocity field, not just the externally imposed velocity field. Since the capillary velocity γ/η is the only local velocity scale, we have

$$\kappa_m = C_\kappa \frac{\eta}{\gamma}\dot{\gamma}, \tag{45}$$

where $C_\kappa=5.13$ is found empirically. The linear relationship (45) is confirmed by Fig. 20, from a fit to which the numerical value of C_κ is also taken. For large extension rates, the curvature becomes practically identical for the two very different geometries under study demonstrating the locality of the flow.

A somewhat less obvious question is whether there is a relationship between κ_m and the flow strength, as measured by the *unperturbed* velocity field (7), evaluated at the tip. However this is indeed the case as shown in Fig. 21; the velocity has been nondimensionalized using the capillary velocity γ/η to give a capillary number. Namely, asymptotically the curvature is well described by

$$\kappa_m = C\exp(a\mathrm{Ca}_{tip}^2), \tag{46}$$

where a appears to be a universal number. This conclusion is supported by the fact that the slope $a=1.6$ is found to be nearly identical for a drop simulation, as shown in Fig. 21. We have also added the experimental data points taken from Fig. 15 to this figure. While the experimental points do not extend far into the asymptotic regime, they are clearly consistent with Eq. (46).

The scaling (46) of the tip curvature disagrees with earlier theoretical estimates for the scale on which the tip becomes rounded [18]. To find this length, Ref. [18] extended Taylor's expansion in the slenderness, presented in Sec. III A, to higher order. To leading order, the rescaled drop profile (21) behaves like $H(\zeta)\approx\frac{1}{2}(1-\zeta)$ near the tip, which is located at $\zeta=1$. The higher-order contributions, confirmed later by [20], are

$$H(\zeta)=\frac{1}{2}(1-\zeta)+B\epsilon^2(1-\zeta)\ln(1-\zeta)+O\epsilon(\epsilon^3), \tag{47}$$

where $\epsilon\propto\mathrm{Ca}^{-3}$ is the slenderness. The higher-order contributions are expected to describe the rounding of the perfectly conical tip. Thus estimating the scale $1-\zeta$ where the next order becomes comparable to the leading order gives

$$1-\zeta\propto\exp(-a_1\epsilon^{-2})\propto\exp(-a_1\mathrm{Ca}^6) \tag{48}$$

for this scale. However, scale (48) suggested by this argument is evidently much smaller than the inverse of curvature (46) found in numerical simulation.

VII. SUMMARY AND CONCLUSIONS

In this paper we investigated the formation of axisymmetric tips in strong flows. In the absence of an inner fluid

($\lambda=0$), neither existing analytical results nor our numerics indicate loss of stability. This permits to investigate the interface shape in the limit of strong flows. In practice, however, the range of accessible capillary number is severely limited by a steep increase in the tip curvature, as seen in Fig. 8, right. Thus even at a moderate capillary numbers of 1/2 the tip of the drop shown in Fig. 5 can no longer be resolved. If on the other hand λ is finite, the tip solution always undergoes a saddle-node bifurcation. The above statements apply to both the drop and the selective withdrawal geometry, and to all external flows studied. The advantage of the drop geometry is its slender shape, so theory is simpler. For the selective withdrawal geometry, on the other hand, more quantitative experimental data are available and axisymmetry is verified more or less exactly.

In the limit of large Ca, assuming $\lambda=0$, the tip region can be split into two parts. First is an *outer* solution described by Taylor's theory. Near the tip (but on scales much larger than κ_m^{-1}) this gives the conical solution (16), whose opening angle is controlled by the balance between surface tension and the outer flow evaluated at the tip. Experiments at very large capillary numbers (up to 10) confirm the slender-body scaling (16) [16]. Good agreement was also found for the limiting case where the tip enters the sink, cf. Fig. 18.

On the scale of the tip size, there exists an *inner* region described by the profile shown in Fig. 19. Numerical evidence shows that it is the same independent of the driving flow and even for very different geometries (a drop or selective withdrawal). However, at the moment there is no theory for the universal tip shape shown in Fig. 19. Note that the tip region cannot be matched directly to the conical outer solution. The latter has an opening angle that depends on Ca, while the opening angle of the former would have to be universal. There is also no theory for the tip curvature given by Eq. (46). This empirical law of course implies that the tip size always remains finite, although in practice it soon reaches molecular scales.

If λ is finite, the tip breaks owing to the interior pressure building up over a finite region near the tip. In agreement with Taylor's theory, valid for small λ, this occurs via a saddle-node bifurcation, even if λ is *not* small [25,41]. For both drops [1] and in the selective withdrawal experiment [5], the structure observed after the bifurcation is a "spout," i.e., a thin jet emanating from the tip. *Unstable* stationary states found beyond the bifurcation are reminiscent of jetting states, but it is not clear the two structures are directly related. While unstable states are surely relevant to the transient dynamics right after the bifurcation, it is not clear that they also correspond to states that develop in the long time limit.

As far as comparison to experiment is concerned, the greatest unresolved question concerns the critical capillary number of the transition in the selective withdrawal experiment [5,6]. In the experiment performed with an air-fluid system, for which λ is 10^{-7}, no transition is ever observed [2], in agreement with the present simulations. In experiments with a two-fluid system, however, the tip curvature at the transition is found to be almost independent of λ, even if λ was varied between 1 and 10^{-3}. As explained in Sec. III B, this is in disagreement with the destabilizing mechanism observed for drops, since the absence of a volume constraint should not play a role. In conclusion, much remains to be done some 70 years after Taylor's original work.

[1] G. I. Taylor, Proc. R. Soc. London, Ser. A **146**, 501 (1934).
[2] S. Courrech du Pont and J. Eggers, Phys. Rev. Lett. **96**, 034501 (2006).
[3] H. A. Stone, Annu. Rev. Fluid Mech. **26**, 65 (1994).
[4] A. M. Gañán-Calvo, Phys. Rev. Lett. **80**, 285 (1998).
[5] I. Cohen and S. R. Nagel, Phys. Rev. Lett. **88**, 074501 (2002).
[6] I. Cohen, Phys. Rev. E **70**, 026302 (2004).
[7] A. M. Gañán-Calvo, R. González-Prieto, P. Riesco-Chueca, M. A. Herrada, and M. Flores-Mosquera, Nat. Phys. **3**, 737 (2007).
[8] R. Suryo and O. A. Basaran, Phys. Fluids **18**, 082102 (2006).
[9] A. M. Gañán-Calvo and J. M. Gordillo, Phys. Rev. Lett. **87**, 274501 (2001).
[10] H. A. Stone, A. D. Stroock, and A. Adjari, Annu. Rev. Fluid Mech. **36**, 381 (2004).
[11] J.-T. Jeong and H. K. Moffatt, J. Fluid Mech. **241**, 1 (1992).
[12] S. Richardson, J. Fluid Mech. **56**, 609 (1972).
[13] H. D. Ceniceros, T. Y. Hou, and H. Si, Phys. Fluids **11**, 2471 (1999).
[14] H. D. Ceniceros and H. Si, J. Comput. Phys. **165**, 237 (2000).
[15] E. O. Tuck and J.-M. V. Broeck, J. Aust. Math. Soc. Ser. B, Appl. Math. **25**, 443 (1984).
[16] C. R. Dun and G. C. Hocking, J. Eng. Math. **29**, 1 (1995).
[17] G. I. Taylor, *Proceedings of the 11th International Congress of Applied Mathematics, Munich, Germany*, edited by H. Görtler (Springer, Heidelberg, 1964), pp. 790–796.
[18] J. D. Buckmaster, J. Fluid Mech. **55**, 385 (1972).
[19] J. D. Buckmaster, J. Fluid Mech. **59**, 481 (1973).
[20] A. Acrivos and T. S. Lo, J. Fluid Mech. **86**, 641 (1978).
[21] E. J. Hinch and A. Acrivos, J. Fluid Mech. **91**, 401 (1979).
[22] J. D. Sherwood, J. Fluid Mech. **144**, 281 (1984).
[23] C. Pozrikidis, J. Fluid Mech. **357**, 29 (1998).
[24] M. Loewenberg and E. J. Hinch, J. Fluid Mech. **321**, 395 (1996).
[25] M. Kleine Berkenbusch, I. Cohen, and W. W. Zhang, J. Fluid Mech. **613**, 171 (2008).
[26] C. Pozrikidis, *Boundary Integral and Singularity Methods for Linearized Flow* (Cambridge University Press, Cambridge, England, 1992).
[27] J. M. Rallison and A. Acrivos, J. Fluid Mech. **89**, 191 (1978).
[28] G. K. Youngren and A. Acrivos, J. Fluid Mech. **76**, 433 (1976).
[29] O. Ladyzhenskaya, *The Mathematical Theory of Viscous Incompressible Flow* (Gordon and Breach, New York, 1969).
[30] W. H. Press, S. A. Teukolski, W. T. Vetterling, and B. P. Flannery, *Numerical Recipes*, 2nd ed. (Cambridge University Press, Cambridge, England, 1992).
[31] J. Happel and H. Brenner, *Low Reynolds Number Hydrody-*

namics (Martinus Nijhoff Publishers, The Hague, 1983).
[32] J. Eggers, Rev. Mod. Phys. **69**, 865 (1997).
[33] D. Barthès-Biesel and A. Acrivos, J. Fluid Mech. **61**, 1 (1973).
[34] J. M. Rallison, Annu. Rev. Fluid Mech. **16**, 45 (1984).
[35] E. J. Hinch, *Perturbation Methods* (Cambridge University Press, Cambridge, 1991).
[36] P. G. Drazin, *Nonlinear Systems* (Cambridge University Press, Cambridge, 1992).
[37] J. Eggers, Phys. Rev. Lett. **86**, 4290 (2001).
[38] J. R. Lister, J. Fluid Mech. **198**, 231 (1989).
[39] S. H. Lee, R. S. Chadwick, and L. G. Leal, J. Fluid Mech. **93**, 705 (1979).
[40] J. Ziegler, J. H. Snoeijer, and J. Eggers, Eur. Phys. J. Special Topics **166**, 177 (2009).
[41] S. C. Case and S. R. Nagel, Phys. Rev. Lett. **98**, 114501 (2007).